The Astrophysical Journal, 632:355–370, 2005 October 10

LINE IMAGING OF ORION KL AT 865 μm WITH THE SUBMILLIMETER ARRAY

H. Beuther, Q. Zhang, L. J. Greenhill, M. J. Reid, D. Wilner, E. Keto,
H. Shinnaga, P. T. P. Ho, and J. M. Moran
Harvard-Smithsonian Center for Astrophysics, 60 Garden Street, Cambridge, MA 02138; hbeuther@cfa.harvard.edu

and

S.-Y. Liu and C.-M. Chang
Academia Sinica Institute of Astronomy and Astrophysics, 1 Roosevelt Road, Section 4, Taipei 106, Taiwan
Received 2005 February 24; accepted 2005 June 23

ABSTRACT

We present the first submillimeter (865 μm) imaging spectral line survey at 1″ resolution conducted with the Submillimeter Array toward Orion KL. Within the 2×2 GHz bandpasses (lower and upper sidebands, 337.2–339.2 and 347.2–349.2 GHz), we find about 145 spectral lines from 13 species, six isotopologues, and five vibrational excited states. Most nitrogen-bearing molecules are strong toward the hot core, whereas the oxygen-bearing molecules peak toward the southwest in the so-called compact ridge. Imaging of spectral lines is shown to be an additional tool to improve the identifications of molecular lines. Arcsecond spatial resolution allows us to distinguish the molecular line emission of the sources *I* and *n* from that of the hot core. The only molecular species detected strongly toward source *I* is SiO, delineating mainly the collimated northeast-southwest low-velocity outflow. The two positions close to source *I*, which have previously been reported to show maser emission in the $v = 0$ ^{28}SiO (1–0) and (2–1) lines, show no detectable maser emission in the $v = 0$ ^{28}SiO (8–7) line at our spatial resolution. SiO is weak toward source *n*, and thus source *n* may not currently be driving a molecular outflow. CH_3OH is the molecule with the highest number of identified lines (46) in this spectral window. This "line forest" allows us to estimate temperatures in the region, and we find temperatures between 50 and 350 K, with the peak temperatures occurring toward the hot core. The detection of strong vibrational excited line emission from the submillimeter continuum peak SMA1 supports the interpretation that the source SMA1 is likely of protostellar nature.

Subject headings: ISM: individual (Orion KL) — ISM: lines and bands — ISM: molecules — stars: formation — submillimeter — techniques: interferometric

1. INTRODUCTION

Orion KL is the most studied region of massive star formation. At a distance of ~450 pc, its molecular spectral line emission is very strong (e.g., Schilke et al. 1997a). Most molecular line studies toward Orion KL have been carried out with single-dish instruments (e.g., Sutton et al. 1985; Blake et al. 1987; Schilke et al. 1997a, 2001; Comito et al. 2005) and thus do not resolve the spatial distribution of the molecular gas. Molecular line studies with interferometers have been conducted only at wavelengths longer than 1 mm (e.g., Wilner et al. 1994; Wright et al. 1996; Blake et al. 1996; Wilson et al. 2000; Liu et al. 2002). While many such studies were single-molecule observations, the first dedicated interferometric line surveys were conducted by Wright et al. (1996) and Blake et al. (1996). The interferometric investigations found that the single-dish spectral features known as the "hot core," "compact ridge," and "plateau" are all associated with the KL region, while the dust continuum source CS1 about 25″ northeast of source *I* exhibits narrower line widths, lower temperatures, and only weak indications of star formation (e.g., Wright et al. 1996).

The hot core as traced by dust continuum emission and nitrogen-bearing molecules such as CH_3CN or NH_3 appears as a chain of dense clumps offset by $\geq 1''$ from the radio source *I*, with estimated temperatures between 130 and 335 K (e.g., Wilner et al. 1994; Wright et al. 1996; Wilson et al. 2000). The compact ridge a few arcseconds southwest of source *I* is reported to have lower temperatures (of the order of 100 K) and to be especially prominent in oxygen-bearing molecules (e.g., Wright et al. 1996; Liu et al. 2002). Furthermore, the region exhibits a complex cluster of infrared sources studied from near- to mid-infrared wavelengths (Dougados et al. 1993; Greenhill et al. 2004; Shuping et al. 2004). At least two outflows are driven from the region on scales $>10^4$ AU, one high-velocity outflow in the southeast-northwest direction observed in molecular lines and in the optical and near-infrared (e.g., Allen & Burton 1993; Wright et al. 1995; Chernin & Wright 1996; Schultz et al. 1999) and one lower velocity outflow in the northeast-southwest direction best traced by thermal SiO and H_2O maser emission, as well as some H_2 bow shocks (e.g., Genzel & Stutzki 1989; Blake et al. 1996; Chrysostomou et al. 1997; Stolovy et al. 1998). The driving source(s) of the outflows are uncertain: initial claims that it might be IRc2 are outdated now, and possible culprits are the radio sources *I* and/or the infrared source *n*, also known as radio source *L* (Menten & Reid 1995). Radio source *I* lies close to the center of the northeast-southwest outflow (Gezari 1992; Menten & Reid 1995; Gezari et al. 1998; Greenhill et al. 2004b) and has not been detected in the near- to mid-infrared (Greenhill et al. 2004a).

A study of the spatial distribution of the different molecular lines can be used to identify and separate different centers of activity via their different excitation conditions. The Submillimeter Array (SMA)[1] on Mauna Kea was dedicated in 2003 November, and Orion was one of its early science targets. Therefore, we present the first high spatial resolution (~450 AU) submillimeter

[1] The Submillimeter Array is a joint project between the Smithsonian Astrophysical Observatory and the Academia Sinica Institute of Astronomy and Astrophysics and is funded by the Smithsonian Institution and the Academia Sinica.

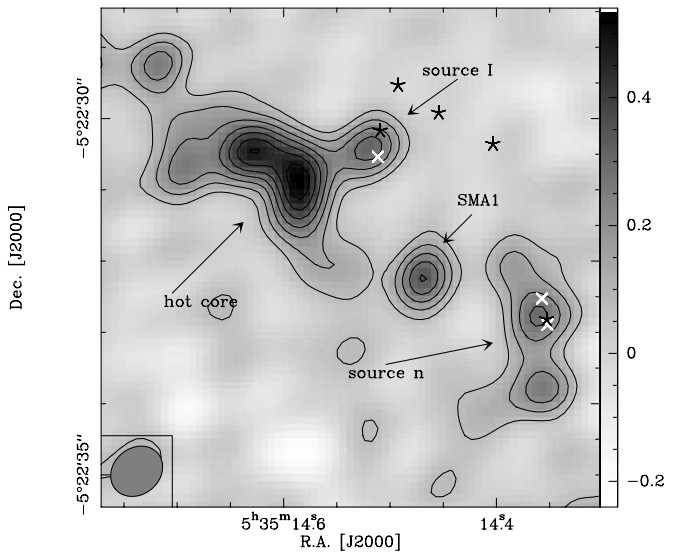

FIG. 1.—Submillimeter continuum image of the Orion KL region at 865 μm (Beuther et al. 2004). The contouring starts at the 2 σ level of 70 mJy beam^{-1} and continues in 2 σ steps. The white crosses mark the radio positions of sources *I* and *n* (two positions for *n* because of its bipolar nature; Menten & Reid 1995). The black stars show the infrared positions of source *n* and IRc2 A–D (Dougados et al. 1993). The synthesized beam is shown at the bottom left (0.″78 × 0.″65). We did not detect any submillimeter continuum feature outside this central region.

wavelength molecular line investigation at 865 μm. Since the data set is incredibly rich, a complete analysis and interpretation of all existing features is beyond the scope of this paper. Here we present the overall content of the data set and focus on a few aspects in more detail. Follow-up investigations are currently undertaken, and the data are publicly available (raw data via the SMA Web site[2] and calibrated data from the lead author of this paper).

The submillimeter continuum emission was presented in a separate paper (Beuther et al. 2004). The continuum data resolved source *I* from the hot core and detected, for the first time, source *n* at a wavelength shorter than 7 mm. Furthermore, a new continuum peak between sources *I* and *n* is found, SMA1, which is either an independent, deeply embedded protostellar object or part of the more extended hot core. These submillimeter continuum sources, reproduced in Figure 1, are used as a reference frame for the discussion of the line emission throughout this paper.

[2] See http://cfa-www.harvard.edu/rtdc/index-sma.html.

2. OBSERVATIONS

Orion KL was observed with the SMA in 2003 December and 2004 February at 348 GHz (865 μm) with seven antennas in two configurations and with projected baselines between 15 and 230 kλ. The phase center was the nominal position of source *I* as given by Plambeck et al. (1995): R.A. (J2000.0) $5^h35^m14^s.50$ and decl. (J2000.0) $-5°22'30''.45$. For bandpass calibration we used Jupiter and Mars. The flux scale was derived from observations of Callisto and is estimated to be accurate to within 15%. Phase and amplitude calibration was done via frequent observations of the quasar 0420−014 about 17° from the phase center. The zenith opacities, measured with the NRAO tipping radiometer located at the Caltech Submillimeter Observatory, were excellent during both tracks with τ(348 GHz) $\sim$ 0.1 and 0.14 [scaled from the 225 GHz measurement via τ(348 GHz) $\sim 2.8\tau$(225 GHz)]. The receiver operated in a double-sideband mode with an intermediate-frequency band of 4–6 GHz, so that the upper and lower sideband were separated by 10 GHz. The correlator had a bandwidth of 2 GHz, and the spectral resolution was 0.8125 MHz. Measured double-sideband system temperatures corrected to the top of the atmosphere were between 250 and 600 K, depending mainly on the elevation of the source.

The *u-v* coverage with no projected baselines below 15 kλ implies that source structure on spatial scales $\geq 13''$ is filtered out by the observations. Interferometric observations of sources close to decl. 0° like Orion KL result in rather poor *u-v*coverage and a dirty beam (Fig. 2), further complicating the image deconvolution. Since there is significant large-scale emission associated with most spectral lines, we deconvolved the point-spread function with the CLEAN algorithm over a large spatial area ($26'' \times 26''$, about $\frac{2}{3}$ of the primary beam size) for each spectral line to derive the final images. It is possible that, for some spectral lines, specific box-cleaning could improve the final images, but this is beyond the scope of this paper. We applied different *u-v* weightings

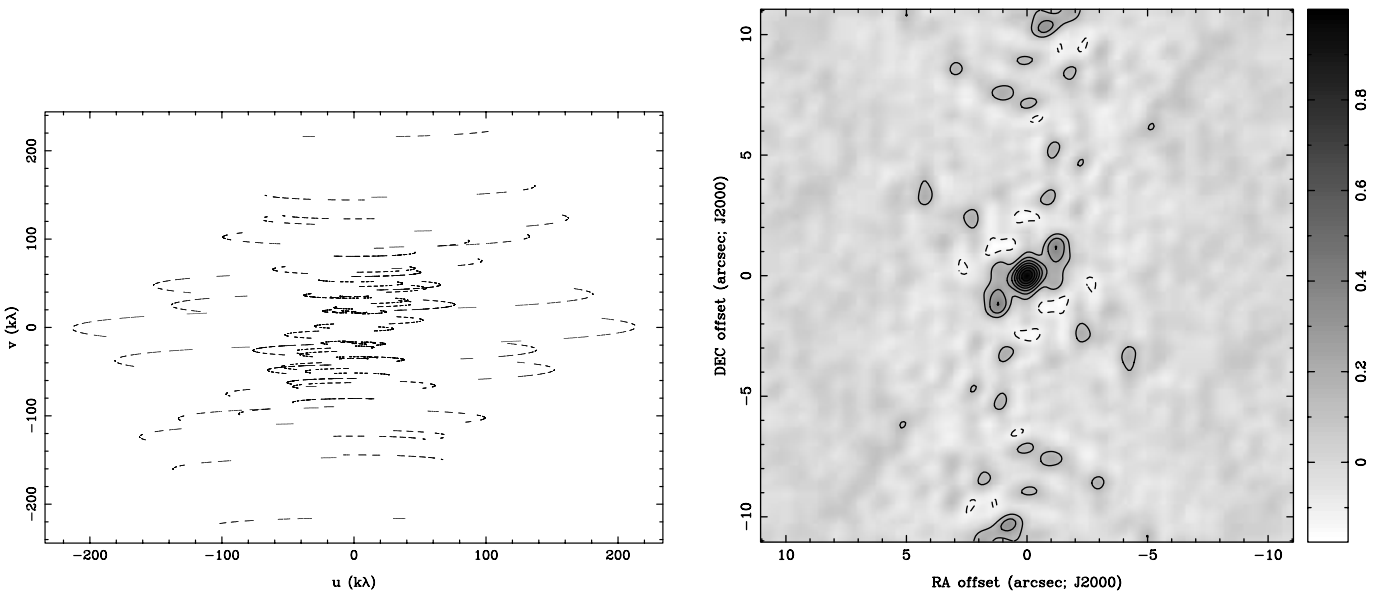

FIG. 2.—*Left*: Resulting *u-v* coverage from the two observed tracks. *Right*: Image of the dirty beam. The contour levels are −0.125 (*dashed line*) and 0.125–1 in 0.125 level steps (*solid lines*).

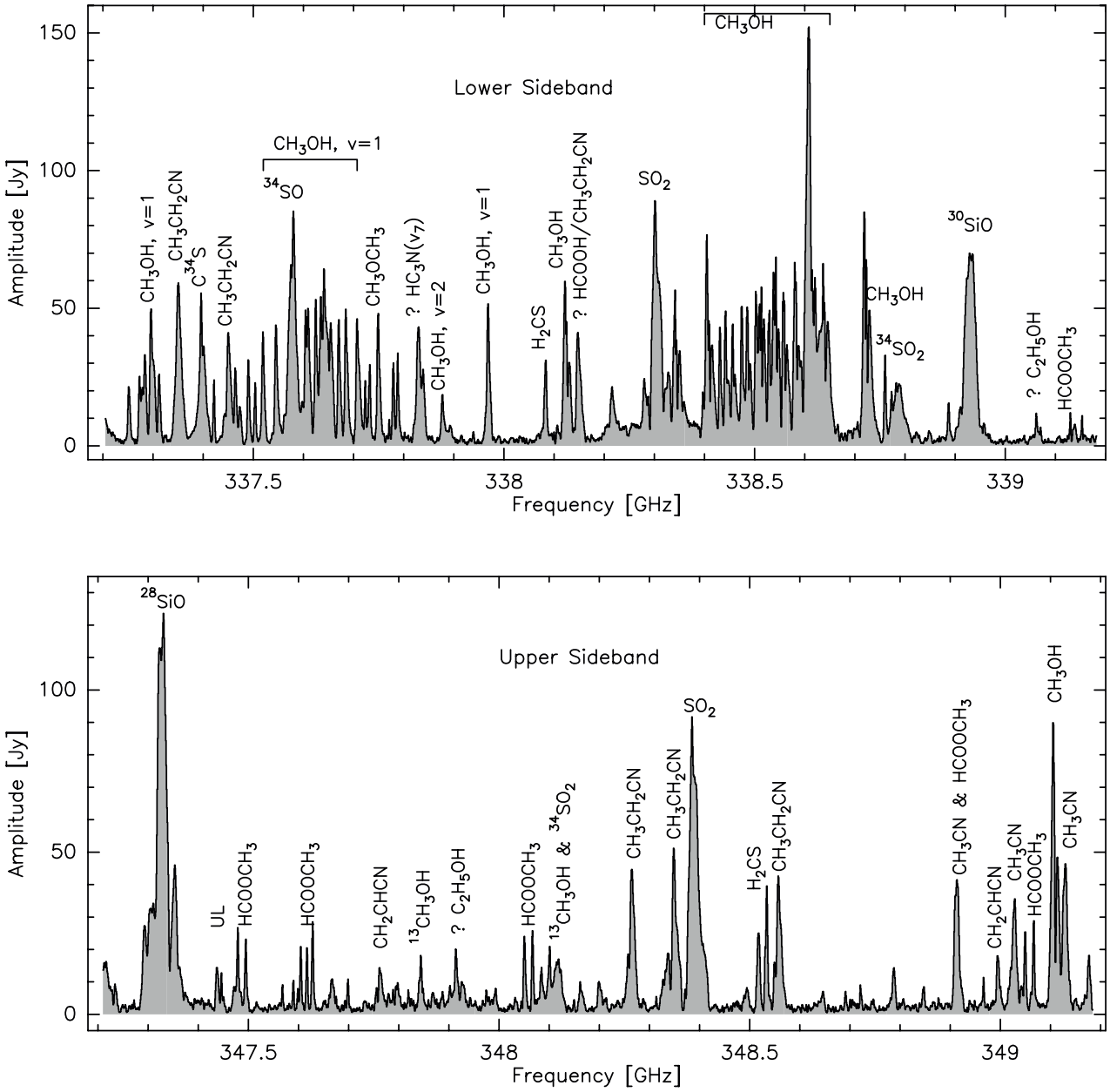

FIG. 3.—Vector-averaged upper and lower sideband spectra in the *u-v* domain on a baseline of ~21 m. UL marks unidentified lines, and question marks indicate only tentatively identified lines.

for various lines, depending mainly on the line strength, and obtained average synthesized beams of $1''.1 \times 0''.9$ (P.A. $-44°$).

To get a feeling for the amount of missing flux, we convolved the data to a $20''$ beam and compared them with the single-dish line survey by Schilke et al. (1997a). Many strong and extended lines have missing flux values up to 90%. For one of our main target lines, ^{28}SiO (8–7), the measured SMA flux is even lower, $\leq$10% of that measured with the Caltech Submillimeter Observatory (CSO; see also the discussion at the end of § 4.1). Since this missing flux has to be distributed over scales $>13''$, possibly as large as the $20''$ beam of the CSO, the missing ^{28}SiO (8–7) flux scaled to the $1''$ synthesized SMA beam can be estimated to approximately 3 Jy beam^{-1}. (For additional discussion on missing flux in particular lines, see §§ 4.1 and 4.2.)

The sensitivity was dynamic range–limited by the sidelobes of the strongest emission peaks and thus varied between the line maps of different molecules and molecular transitions. This limitation was due to the incomplete sampling of short *u-v* spacings and the presence of extended structures. The theoretical 1 σ rms per 1 km s^{-1} channel was ~100 mJy, whereas the measured 1 σ rms in a 1 km s^{-1} channel image was of the order of 500 mJy because of the dynamic-range problem and thus insufficient cleaning. The 1 σ rms for the velocity-integrated molecular line maps (the velocity ranges for the integrations were chosen for each line separately, depending on the line widths and intensities) ranged between 70 and 320 mJy with a mean 1 σ value of ~170 mJy. We calibrated the data within the IDL superset MIR developed for the Owens Valley Radio Observatory and adapted for the SMA; the imaging was performed in MIRIAD. For more details on the array and its capabilities, see Ho et al. (2004).

3. RESULTS

Figure 3 presents the whole observed bandpass with its extremely rich line forest; a closer zoom into each sideband is

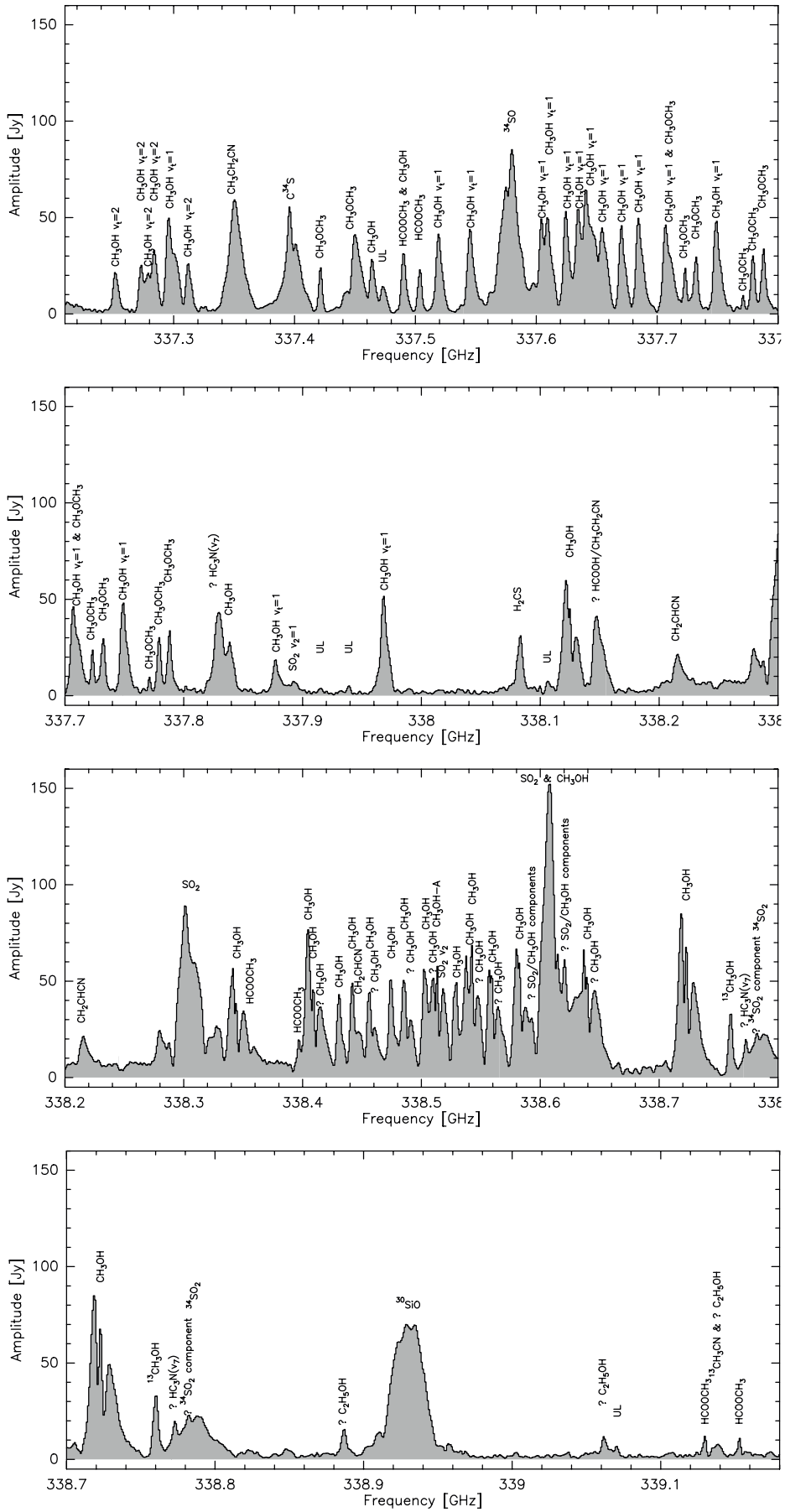

FIG. 4.—Vector-averaged lower sideband spectra (ZOOM) in the *u-v* domain on a short baseline of ∼21 m. The spectral resolution is 0.7 km s^{-1}. UL marks unidentified lines, and question marks indicate only tentatively identified lines.

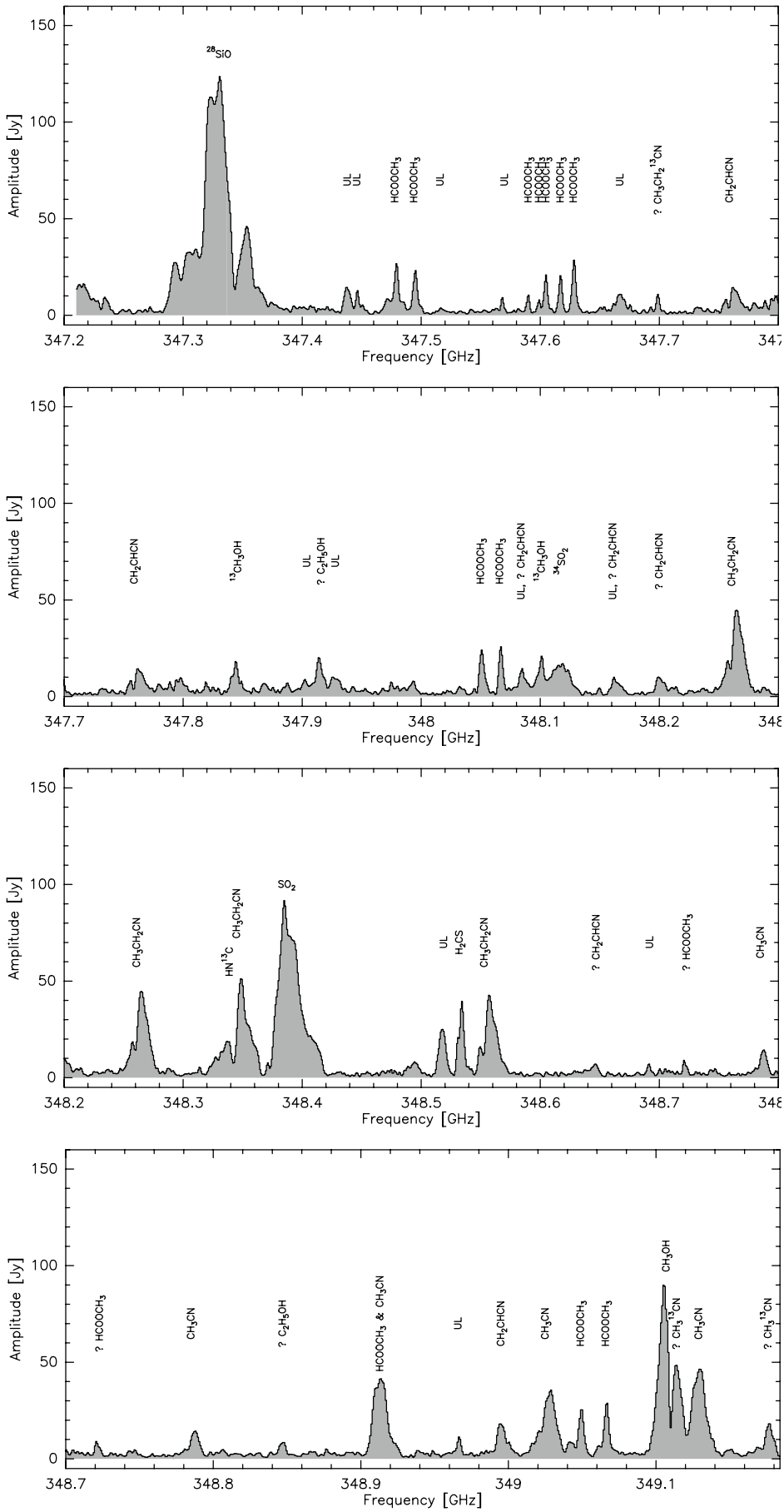

FIG. 5.—Same as Fig. 4, but for the upper sideband.

TABLE 1

OBSERVED LINES

ν (GHz)	Line
337.252	CH_3OH ($7_{5,2}-6_{5,2}$) A ($v_t = 2$)
337.274	CH_3OH ($7_{6,2}-6_{5,1}$) A ($v_t = 2$)
337.279	CH_3OH ($7_{3,5}-6_{2,4}$) E ($v_t = 2$)
337.284	CH_3OH ($7_{4,4}-6_{3,3}$) A ($v_t = 2$)
337.297	CH_3OH ($7_{4,3}-6_{4,3}$) A ($v_t = 1$)
337.312	CH_3OH ($7_{3,4}-6_{3,4}$) A ($v_t = 2$)
337.348	CH_3CH_2CN ($38_{3,36}-37_{3,35}$)
337.397	$C^{34}S$(7–6)
337.421	CH_3OCH_3 ($21_{2,19}-20_{3,18}$)
337.446	CH_3CH_2CN ($37_{4,33}-36_{4,32}$)
337.464	CH_3OH ($7_{7,1}-6_{6,0}$) A
337.473	UL
337.490	$HCOOCH_3$ ($27_{8,20}-26_{8,19}$) E and CH_3OH ($7_{1,7}-6_{0,6}$) E
337.503	$HCOOCH_3$ ($27_{8,20}-26_{8,19}$) A
337.519	CH_3OH ($7_{5,2}-6_{5,2}$) E ($v_t = 1$)
337.546	CH_3OH ($7_{6,1}-6_{6,1}$) A ($v_t = 1$)
337.580	^{34}SO (8_8-7_7)
337.605	CH_3OH ($7_{3,5}-6_{2,4}$) E ($v_t = 1$)
337.611	CH_3OH ($7_{2,5}-6_{2,5}$) E ($v_t = 1$)
337.626	CH_3OH ($7_{5,3}-6_{4,2}$) A^+ ($v_t = 1$)
337.636	CH_3OH ($7_{5,3}-6_{4,2}$) A^- ($v_t = 1$)
337.642	CH_3OH ($7_{4,3}-6_{4,3}$) A ($v_t = 1$)
337.644	CH_3OH ($7_{4,4}-6_{3,3}$) E ($v_t = 1$)
337.646	CH_3OH ($7_{2,6}-6_{1,5}$) A ($v_t = 1$)
337.648	CH_3OH ($7_{1,6}-6_{1,6}$) A ($v_t = 1$)
337.655	CH_3OH ($7_{5,2}-6_{5,2}$) A ($v_t = 1$)
337.671	CH_3OH ($7_{5,3}-6_{4,2}$) A ($v_t = 1$)
337.685	CH_3OH ($7_{6,1}-6_{6,1}$) A ($v_t = 1$)
337.708	CH_3OH ($7_{3,4}-6_{3,4}$) A ($v_t = 1$)
337.712	CH_3OCH_3 ($7_{4,4}-6_{3,3}$) EA
337.722	CH_3OCH_3 ($7_{4,4}-6_{3,3}$) EE
337.732	CH_3OCH_3 ($7_{4,3}-6_{3,3}$) EE
337.749	CH_3OH ($7_{4,4}-6_{3,3}$) A ($v_t = 1$)
337.771	CH_3OCH_3 ($7_{4,4}-6_{3,4}$) EA
337.778	CH_3OCH_3 ($7_{4,4}-6_{3,4}$) EE
337.787	CH_3OCH_3 ($7_{4,3}-6_{3,4}$) AA
337.830	HC_3N (37–36) ($v_7 = 1$)@337.825?
337.838	CH_3OH ($20_{6,14}-21_{5,15}$)
337.878	CH_3OH ($7_{4,3}-6_{4,3}$) A ($v_t = 2$)
337.892	SO_2 ($21_{2,20}-21_{1,21}$) $v_2 = 1$
337.915	UL
337.939	UL
337.969	CH_3OH ($7_{4,3}-6_{4,3}$) A ($v_t = 1$)
338.081	H_2CS ($10_{1,10}-9_{1,9}$)
338.106	UL
338.125	CH_3OH ($7_{4,4}-6_{3,3}$) E
338.144	CH_3CH_2CN ($37_{3,34}-36_{3,33}$)
338.214	CH_2CHCN ($37_{1,37}-36_{1,36}$)
338.306	SO_2 ($14_{4,14}-18_{3,15}$), many comp.
338.345	CH_3OH ($7_{4,0}-6_{3,4}$) E
338.356	$HCOOCH_3$ ($27_{8,19}-26_{8,18}$) A
338.396	$HCOOCH_3$ ($27_{7,21}-26_{7,20}$) E
338.405	CH_3OH ($7_{7,1}-6_{6,0}$) E
338.409	CH_3OH ($7_{4,4}-6_{3,3}$) A
338.415	Part of CH_3OH ($7_{4,4}-6_{3,3}$) A?
338.431	CH_3OH ($7_{1,7}-6_{0,6}$) E
338.442	CH_3OH ($7_{7,1}-6_{0,0}$) A
338.448	CH_2CHCN ($37_{0,37}-36_{0,36}$)
338.457	CH_3OH ($7_{1,6}-6_{1,6}$) E
338.461	Part of CH_3OH ($7_{1,6}-6_{1,6}$) E?
338.475	CH_3OH ($7_{6,1}-6_{6,1}$) E
338.486	CH_3OH ($7_{6,1}-6_{6,1}$) A
338.491	Part of CH_3OH ($7_{6,1}-6_{6,1}$) A?

TABLE 1—*Continued*

ν (GHz)	Line
338.504	CH_3OH ($7_{2,6}-6_{1,5}$) E
338.510	Part of CH_3OH ($7_{2,6}-6_{1,5}$) E?
338.513	CH_3OH ($7_{6,2}-6_{5,1}$) A
338.517	SO_2 ($55_{6,50}-54_{7,47}$) $v_2 = 1$
338.530	CH_3OH ($7_{6,2}-6_{5,1}$) E
338.541	CH_3OH ($7_{5,2}-6_{5,2}$) A^+
338.543	CH_3OH ($7_{5,2}-6_{5,2}$) A^-
338.547	Part of CH_3OH ($7_{5,2}-6_{5,2}$) A^-?
338.560	CH_3OH ($7_{2,5}-6_{2,5}$) E
338.565	Part of CH_3OH ($7_{2,5}-6_{2,5}$) E?
338.583	CH_3OH ($7_{5,2}-6_{5,2}$) E
338.587	Part of SO_2/CH_3OH?
338.592	Part of SO_2/CH_3OH?
338.607	Part of SO_2/CH_3OH?
338.612	SO_2 ($20_{1,19}-19_{2,18}$)
338.615	CH_3OH ($7_{4,3}-6_{4,3}$) E
338.621	Part of CH_3OH ($7_{4,3}-6_{4,3}$) E?
338.640	CH_3OH ($7_{5,3}-6_{4,2}$) A
338.646	Part of CH_3OH ($7_{5,3}-6_{4,2}$) A?
338.723	CH_3OH ($7_{3,5}-6_{2,4}$) E
338.729	Part of CH_3OH ($7_{3,5}-6_{2,4}$) E?
338.760	$^{13}CH_3OH$ ($13_{7,7}-12_{7,6}$) A
338.772	HC_3N (37–36) ($v_7 = 2$)@338.768?
338.782	Part of $^{34}SO_2$ ($14_{4,10}-14_{3,1}$)?
338.786	$^{34}SO_2$ ($14_{4,10}-14_{3,1}$)
338.884	C_2H_5OH ($15_{7,9}-15_{6,10}$)?[b]
338.930	^{30}SiO (8–7), broad line
339.058	C_2H_5OH ($14_{7,7}-14_{6,8}$)?[b]
339.071	UL
339.129	$HCOOCH_3$ ($13_{7,7}-12_{6,7}$) E
339.138	$^{13}CH_3CN$ ($19_{6,19}-18_{6,18}$)@339.137 and C_2H_5OH ($27_{7,20}-27_{3,24}$)@339.141?[b]
339.153	$HCOOCH_3$($13_{7,6}-12_{6,6}$) E
347.331	^{28}SiO (8–7), broad line
347.438	UL
347.446	UL
347.478	$HCOOCH_3$ ($27_{1,26}-26_{1,25}$) E
347.494	$HCOOCH_3$ ($27_{5,22}-26_{5,21}$) A
347.516	UL
347.570	UL
347.590	$HCOOCH_3$ ($16_{6,10}-15_{5,11}$) A
347.599	$HCOOCH_3$ ($16_{6,10}-15_{5,11}$) E
347.605	$HCOOCH_3$ ($28_{10,18}-27_{10,17}$) E
347.617	$HCOOCH_3$ ($28_{10,19}-27_{10,18}$) A
347.628	$HCOOCH_3$ ($28_{10,19}-27_{10,18}$) E
347.667	UL
347.699	$CH_3CH_2^{13}CN$ ($9_{8,1}-9_{7,2}$)?
347.759	CH_2CHCN ($36_{2,34}-35_{2,32}$)
347.846	$^{13}CH_3OH$ ($21_{12,9}-20_{12,8}$) A
347.903	UL
347.916	C_2H_5OH ($20_{4,17}-19_{4,16}$)?[b]
347.928	UL
348.050	$HCOOCH_3$ ($28_{4,24}-27_{4,23}$) E
348.066	$HCOOCH_3$ ($28_{6,23}-27_{6,22}$) A
348.084	UL, CH_2CHCN ($57_{2,55}-58_{0,58}$)?
348.101	$^{13}CH_3OH$ ($11_{6,6}-10_{6,5}$) E
348.118	$^{34}SO_2$($19_{4,16}-19_{3,17}$)
348.161	UL, CH_2CHCN ($38_{0,38}-37_{0,37}$)?
348.200	CH_2CHCN ($25_{7,19}-26_{6,20}$)?
348.261	CH_3CH_2CN ($39_{2,37}-38_{2,36}$)
348.340	$HN^{13}C$(4–3), blended
348.345	CH_3CH_2CN ($40_{2,39}-39_{2,38}$), blended
348.388	SO_2($24_{2,22}-23_{3,21}$)
348.519	UL,[a] HNOS($1_{1,1}-2_{0,2}$)@348.518?

TABLE 1—*Continued*

ν (GHz)	Line
348.532	$H_2CS(10_{1,9}-9_{1,8})$
348.553	CH_3CH_2CN $(40_{1,39}-39_{1,38})$
348.647	CH_2CHCN $(20_{4,17}-21_{2,20})$?
348.692	UL
348.723	$HCOOCH_3$ $(28_{9,20}-27_{9,18})$ E?
348.785	CH_3CN $(19_{10}-18_{10})$
348.847	C_2H_5OH $(10_{6,4}-9_{5,4})$?[b]
348.910	$HCOOCH_3$ $(28_{9,20}-27_{9,19})$ E
348.911	CH_3CN (19_9-18_9)
348.915	$HCOOCH_3$ $(28_{9,20}-27_{9,19})$ A
348.966	UL
348.991	CH_2CHCN $(37_{1,36}-36_{1,35})$
349.025	CH_3CN (19_8-18_8)
349.049	$HCOOCH_3$ $(28_{9,19}-27_{9,18})$ E
349.066	$HCOOCH_3$ $(28_{9,19}-27_{9,17})$ A
349.107	CH_3OH $(14_{8,7}-14_{7,7})$
349.114	$CH_3{}^{13}CN$ (19_5-18_5)?
349.125	CH_3CN (19_7-18_7)
349.173	$CH_3{}^{13}CN$ (19_4-18_4)?

NOTES.—Question marks indicate those lines that are only tentatively identified. UL: Unidentified line.

[a] The spatial distributions resembles nitrogen-bearing molecules like CH_3CN.

[b] The spatial distributions of the C_2H_5OH emission are not the same for all lines. Thus, some are probably misassigned; it is difficult to judge which.

shown in Figures 4 and 5. The line identifications are not always unambiguous because different velocity components and large line widths are present in the region. At first, the lines were identified by comparing our spectra with those of the previous single-dish study of Schilke et al. (1997a). Then, in selected cases we used the JPL, CDMS, and LOVAS line catalogs (Poynter & Pickett 1985; Müller et al. 2001; Lovas 2004) for confirmations and further identifications. Altogether, we find about 145 lines above an approximate flux level of 8 Jy on the short baseline of 21 m (Figs. 3, 4, and 5). We note that this is not the sensitivity limit of the data but rather a cutoff below which confusion becomes an even larger problem and line identifications get considerably more difficult. Of the 145 lines listed in Table 1, we are able to identify approximately 90%. Tentative identifications are marked in Table 1 and Figures 3, 4, 5, and 6 with question marks.

In addition to the listed lines, especially the upper sideband data (Fig. 5) show many features at low intensities, of which a majority are likely not noise but consists of weak additional spectral lines. At the given noise level, we do not investigate these features any further, but it is likely that finding real line-free spectral regions to study the pure continuum emission in such hot core type sources is difficult. The produced continuum emission will mostly be "polluted" by underlying weak line emission. As outlined below and in Beuther et al. (2004), imaging of the lines helps significantly. For example, source *I* is nearly line-free (except for SiO), and thus the continuum emission is reliable, whereas this is less likely the case for the hot core region. To get an estimate of the line contamination, we produced a second pseudo-continuum image averaging the whole upper sideband data (in contrast to the continuum image presented in Beuther et al. [2004] and Fig. 1, where we excluded all strong lines from the upper sideband). We did not use the lower sideband data because the line contamination there is significantly higher due to the strong CH_3OH bands. Deriving the source peak flux values from this new image for each continuum subsource, the values are only 5%–10% higher than those for the original image. While the original image still covers a considerable bandpass of the upper sideband with low-level emission, it is unlikely that the low-level emission exceeds the contribution of the strong lines in the bandpass. Therefore, we estimate the continuum flux uncertainties due to line contamination in the image presented in Beuther et al. (2004) and Figure 1 to be $<10\%$, independent of the subsources. This is well within our calibration uncertainties of 15% (§ 2). We note that this line contamination estimate is only valid for this particular data set and cannot be extrapolated to single-dish studies, because the spatial filtering for the line and continuum data with the interferometer varies and single-dish bolometers cover a significantly larger bandwidth (e.g., $\sim$80 GHz for the MAMBO array; Kreysa et al. 1998)

Fifteen percent of the lines listed in Table 1 were not reported in the previous single-dish survey (Schilke et al. 1997a), not to mention the additional low-level emission. In contrast, we do not identify any clear interferometric nondetection of a previously detected single-dish line, which could occur for very broadly distributed molecular gas, implying that most molecular emission must have some compact components.

Many of the lines listed in Table 1 can be attributed to a few molecules, and we identify 13 different species, six isotopologues, and five vibrational excited states within the data set (Table 2). Most of these have clearly separated lines without much blending and thus can be imaged. Choosing one of the strongest lines of each species, we produced velocity-integrated images of each. Figure 6 presents a compilation of line images from representative species in the data set (see Table 3). A first inspection of these line images highlights the following interesting characteristics:

1. The main molecular species detected toward source *I* is SiO. It clearly delineates the known low-velocity northeast-southwest outflow. Other species are either not detected toward source *I* (e.g., CH_3OH) or exhibit only weak emission (e.g., SO_2).
2. Most emission from nitrogen-bearing species is strong toward the hot core and has a similar morphology to NH_3 (Wilson et al. 2000). This confirms previous results at lower frequencies by Wright et al. (1996) and Blake et al. (1996).
3. Most oxygen-bearing molecules are weaker toward the hot core but stronger in the southwest toward the so-called compact ridge[3] (see also Wright et al. 1996).
4. Sulphur-bearing species show emission toward the hot core and the compact ridge (see also Wright et al. 1996). Vibrationally excited lines are stronger toward the hot core and SMA1.
5. Both oxygen- and sulphur-bearing molecules show additional emission toward the northwest, spatially associated with IRc6. Millimeter continuum emission from this region has been previously reported by Blake et al. (1996).
6. The imaging of the molecular lines allows a better identification of the spectral lines. For example, the previous identification of the HCOOH $(15_{4,12}-14_{4,11})$ line at 338.144 GHz (Schilke et al. 1997a) is called into question because its spatial structure resembles that of an N-bearing rather than an O-bearing species. Its spatial distribution also appears different from its 1 mm counterpart presented in Liu et al. (2002). Therefore, this line is more likely $CH_3CH_2CN(37_{3,34}-36_{3,33})$. Some of the tentative identifications in Table 1 and Figures 3, 4, 5, and 6 are uncertain due to this as well.

Another way to study the spatial differences of the molecular line emission is via extraction of spectra from the whole spectral

[3] The "compact ridge" has no clearly defined peak positions but extends $5''-10''$ in the east-west direction with peak positions varying with the molecular line transitions (see Fig. 6).

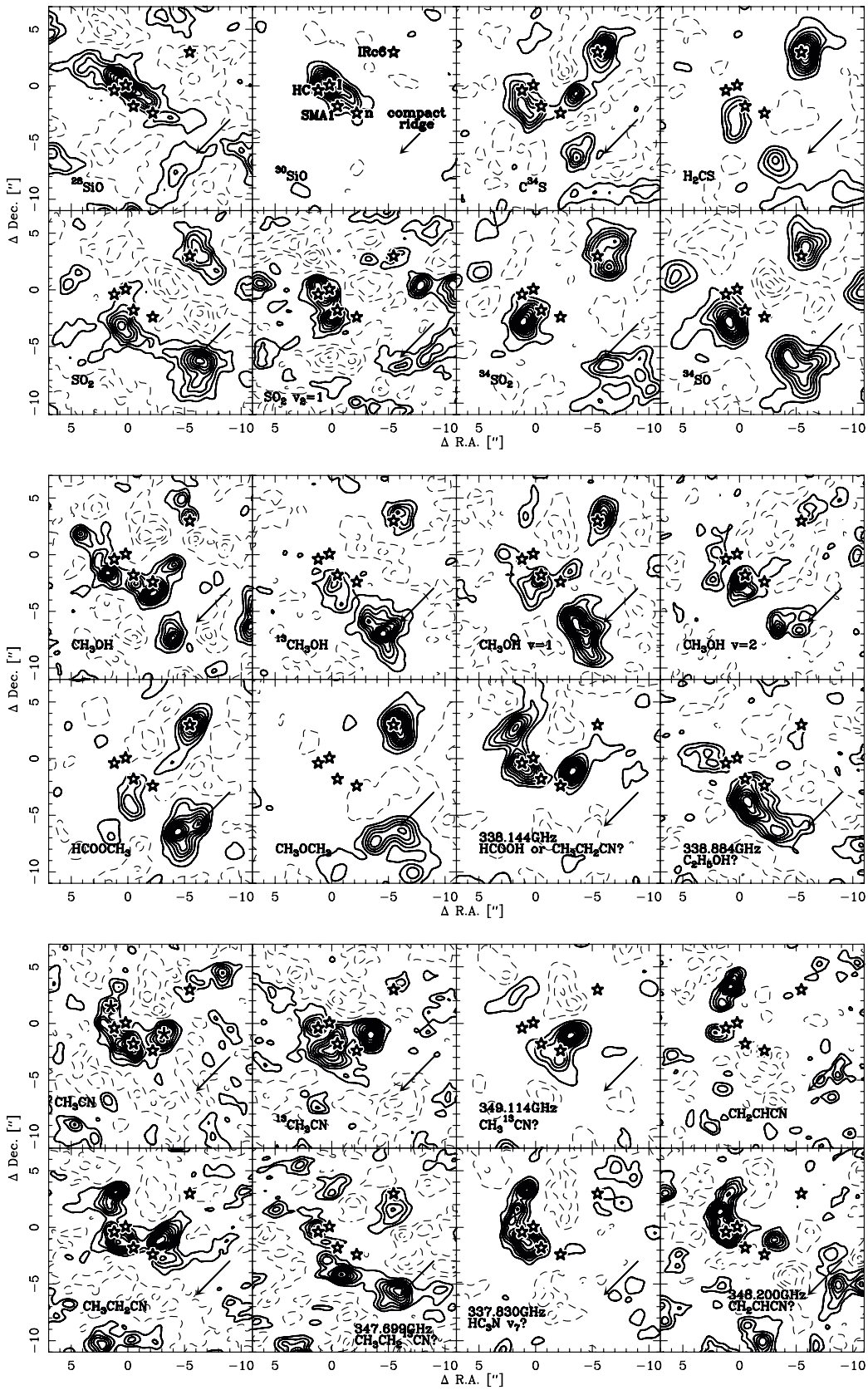

FIG. 6.—Continuum-subtracted images of molecular species. The thick contours present the molecular emission (labeled in each panel) from 10% to 90% (steps of 10%) of each species' peak emission. Additional parameters for each line image are given in Table 3. The axes are offsets in the directions of right ascension and declination. The dashed contours show the negative emission from 10% to 90% (steps of 20%), which is due to missing short spacings. Source *I*, the hot core (HC), SMA1, source *n*, IRc6, and the compact ridge are marked in each panel and labeled in the ^{30}SiO panel (*top row, second panel*). Two additional CH_3CN positions, where spectra are shown from in Fig. 7, are marked with two additional stars in the CH_3CN panel. The top two rows show the Si- and and S-bearing species, the middle two rows present the OH-bearing molecules, and the bottom two rows focus on the N-bearing species. Question marks indicate those lines with tentative or uncertain identifications (see Tables 1 and 3).

TABLE 2
DETECTED MOLECULAR SPECIES

Species	Isotopologues	Vibrational States
^{28}SiO	^{30}SiO	
$C^{34}S$		
^{34}SO		
SO_2	$^{34}SO_2$	$SO_2 v_2 = 1$
$HN^{13}C$		
H_2CS		
		HC_3N $v_7 = 1, 2$?
CH_3OH	$^{13}CH_3OH$	CH_3OH $v_t = 1,\ 2$
CH_3CN	$^{13}CH_3CN$	
	$CH_3{}^{13}CN$?	
CH_2CHCN		
$HCOOCH_3$		
CH_3OCH_3		
C_2H_5OH		
CH_3CH_2CN	$CH_3CH_2{}^{13}CN$?	

NOTE.—Question marks indicate those species that are only tentatively identified.

data cube at selected positions within the field of view. For this purpose, we imaged the large data cube with a lower spectral resolution of 3 km s^{-1} and extracted spectra toward the positions of source *I*, source *n*, the hot core, SMA1, three CH_3CN peak positions, the southern CH_3OH peak position, the prominent western gas peak, and the most northern peak, which is strong in HC_3N (Fig. 7).

The most striking difference appears to be between source *I* and most of the other positions. Toward source *I*, only ^{28}SiO and its rarer isotopologue ^{30}SiO are strong, whereas toward the other positions many more lines are detected but SiO is weaker. The hot core and SMA1, as well as the CH_3CN peak positions, are all strong line emitters. Regarding CH_3OH, the strongest and most prominent position is the southern peak associated with the compact ridge. It shows the strongest CH_3OH line bands in the ground state, as well as the vibrationally excited states. The northwestern peak is still rather strong in the ground state CH_3OH lines, but the vibrationally excited bands are significantly weaker than those toward the southern peak.

A comparison of these different spectra shows the necessity of high spatial resolution in such complex regions. At lower angular resolution, the complexity of spatial variations and different excitation conditions blends together and results in integrated spectra, as seen in many single-dish studies and also in Figure 3.

4. ANALYSIS AND DISCUSSION

4.1. ^{28}SiO (8–7) *and* ^{30}SiO (8–7)

The main ^{28}SiO (8–7) line was one of our prime target lines within this survey. Previous studies of the lower excitation ground state ^{28}SiO lines showed that in Orion KL, SiO traces the collimated northeast-southwest outflow, as well as the less-collimated structures in the northwest-southeast direction (Chandler & de Pree 1995; Wright et al. 1995; Blake et al. 1996). A peculiarity of the ^{28}SiO $v = 0$ emission is that the (1–0) and the (2–1) lines show maser emission in a bow tie–like structure close to source *I* (Chandler & de Pree 1995; Wright et al. 1995). The orientation of the bow-tie is along the axis of the northeast-southwest outflow; its two peak positions are approximately 0.″5 offset from source *I* in both directions. The ^{28}SiO (5–4) observations of Blake et al. (1996) lacked the spatial resolution to disentangle the potential maser positions from the other SiO emission, but at their

TABLE 3
LINE IMAGE PARAMETERS TO FIGURE 6

Line	E_{upper} (K)	v_{low}, v_{high} (km s^{-1})	S_{peak} (Jy)
^{28}SiO (8–7)	75	−20, 40	2.1
^{30}SiO (8–7)	73	−12, 28	4.0
$C^{34}S$ (7–6)	65	−2, 14	2.4
H_2CS ($10_{1,10}$–$9_{1,9}$)	105	2, 10	3.4
SO_2 ($24_{2,22}$–$23_{3,21}$)	293	−10, 20	2.3
SO_2 ($21_{2,20}$–$21_{1,21}$) ($v_2 = 1$)	965	4, 10[a]	0.6
$^{34}SO_2$ ($19_{4,16}$–$19_{3,17}$)	213	3, 13	1.6
^{34}SO (8_8–7_7)	86	1, 15	3.3
CH_3OH ($7_{5,2}$–$6_{5,2}$) E	112	2, 6[a]	3.3
$^{13}CH_3OH$ ($13_{7,7}$–$12_{7,6}$) A	206	4, 12	2.0
CH_3OH ($7_{4,3}$–$6_{3,3}$) A ($v_t = 1$)	390	3, 13	2.8
CH_3OH ($7_{5,2}$–$6_{5,2}$) A ($v_t = 2$)	722	4, 12	1.6
$HCOOCH_3$ ($28_{10,19}$–$27_{10,18}$)	307	4, 10	2.6
CH_3OCH_3 ($7_{4,3}$–$6_{3,3}$) EE	48	5, 10	3.3
HCOOH ($15_{4,12}$–$14_{4,11}$)[b] or CH_3CH_2CN ($37_{3,34}$–$36_{3,33}$)	181	0, 8	3.0
?C_2H_5OH ($15_{7,9}$–$15_{6,10}$)	162	3, 7	1.1
CH_3CN (19_8–18_8)	624	1, 9	2.0
$^{13}CH_3CN$ ($19_{6,19}$–$18_{6,18}$)	420	4, 10[a]	0.9
?$CH_3{}^{13}CN$ (19_5–18_5)	346	2, 10	5.1
CH_2CHCN ($37_{1,37}$–$36_{1,36}$)	312	2, 10	1.7
CH_3CH_2CN ($39_{2,37}$–$38_{2,36}$)	344	−4, 12	1.3
?$CH_3CH_2{}^{13}CN$ ($9_{8,1}$–$9_{7,2}$)	90	6, 12	0.9
?HC_3N (37–36) ($v_7 = 1$)	628	1, 11	2.4
?CH_2CHCN ($25_{7,19}$–$26_{6,20}$)	746	6, 11	1.0

NOTE.—Question marks indicate those species that are only tentatively identified.
[a] Small integration ranges to avoid line blending.
[b] See § 3 and Fig. 6 for a discussion.

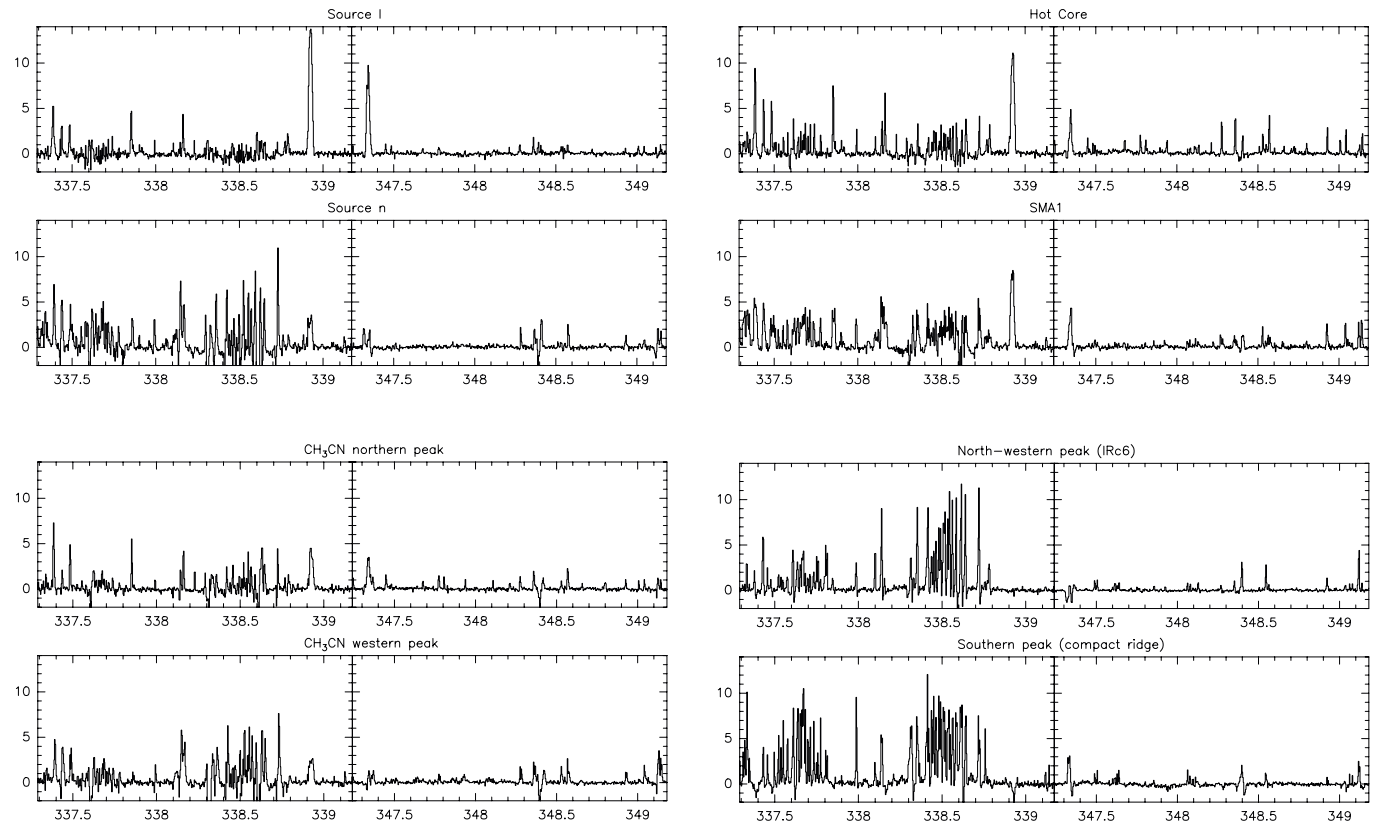

FIG. 7.—Spectra taken toward selected positions after imaging the whole data cube; the spectral resolution is smoothed to 3 km s^{-1}. The spatial positions are marked in Fig. 6. The *x*-axis shows the frequency (GHz), and the *y*-axis shows the amplitude (Jy). Negative features are not real but caused by missing short spacings. The positive emission is affected by the missing short spacings as well.

given spatial resolution they do not find extremely high brightness temperatures that would imply obvious ^{28}SiO (5–4) maser emission. We now resolve the potential maser positions better in the ^{28}SiO (8–7) line, but we also do not find any indication for ^{28}SiO (8–7) maser emission toward these positions.

However, there is thermal ^{28}SiO (8–7) and ^{30}SiO (8–7) emission on larger spatial scales tracing the molecular outflows. Figures 8 and 9 show channel maps of the ^{28}SiO and ^{30}SiO (8–7) data. While the velocity range from -5 to 20 km s^{-1} is dominated by the collimated northeast-southwest outflow, the higher velocity channels, especially those of ^{28}SiO (8–7), also show more extended emission. We stress that the ^{28}SiO (8–7) emission suffers strongly from missing short spacings and thus sidelobe problems. In particular, the northeast-southwest stripes at the edges of the field presented in the ^{28}SiO (8–7) channel map (Fig. 8, *middle row*) are sidelobe emission and not real. Comparing the channel maps with a vector-averaged ^{28}SiO (8–7) spectrum (Fig. 10), one finds that the collimated and the extended emission features are clearly separated in the spectrum as well. The more extended features are represented by the secondary peaks at <-5 and >20 km s^{-1}, whereas the collimated northeast-southwest structure is confined to the lower velocities in between.

To investigate the different distributions, we averaged the ^{28}SiO (8–7) emission over the red and blue secondary peaks, the red and blue collimated outflow, and the central velocities. The final images are presented in Figure 11. We used the main isotopologue for this purpose because, even considering the short spacings problems, it is more sensitive to the larger scale emission. The collimated structures at low to intermediate velocities are similar for both isotopologues. Obviously, the central velocities are dominated by the collimated outflow (Fig. 11, *left*). Going to slightly higher velocities, we find blue and red emission toward the southwest and northeast of source *I* (Fig. 11, *middle*). Since we resolve the outflow spatially well in the northeast-southwest direction and still find significant overlap of blue and red emission on both sides of source *I*, this indicates that the outflow is likely close to the plane of the sky. (For an outflow orientation that is close to the plane of the sky, expanding outflow lobes along the line of sight produce the observed red and blue signature.) Going to the higher velocity secondary peaks (Fig. 11, *right*), the emission is more extended and spatially consistent with previous ^{28}SiO (2–1) observations by Wright et al. (1995). The blue emission might be part of the larger scale northwest-southeast outflow, but the signature of the red higher velocity ^{28}SiO emission is less clear. It shows emission toward the southeast as expected from the large-scale outflow, but it has additional emission toward the southwest as well. As already mentioned, the ^{28}SiO emission suffers from missing flux problems due to the missing short spacings (Figs. 8 and 11), and it is difficult to interpret the large-scale emission in more detail.

Source *n* might be the driver of one of the outflows in the region (e.g., Menten & Reid 1995). However, source *n* is a strong near-infrared source and thus not deeply embedded and not particularly young. In addition, source *n* is weak in the usual outflow-tracing SiO emission (Figs. 6 and 7), which might be indicative of a lack of recent molecular outflow activity. In contrast to this, there is evidence indicating a potential outflow from source *n* based on radio, H_2O maser, and infrared emission signatures (e.g., Menten & Reid 1995; Stolovy et al. 1998; Greenhill et al. 2004a; Shuping et al. 2004). While the SiO emission often traces molecular outflows (e.g., Schilke et al. 1997b; Gueth & Guilloteau 1999; Cesaroni et al. 1999), the SiO nondetection

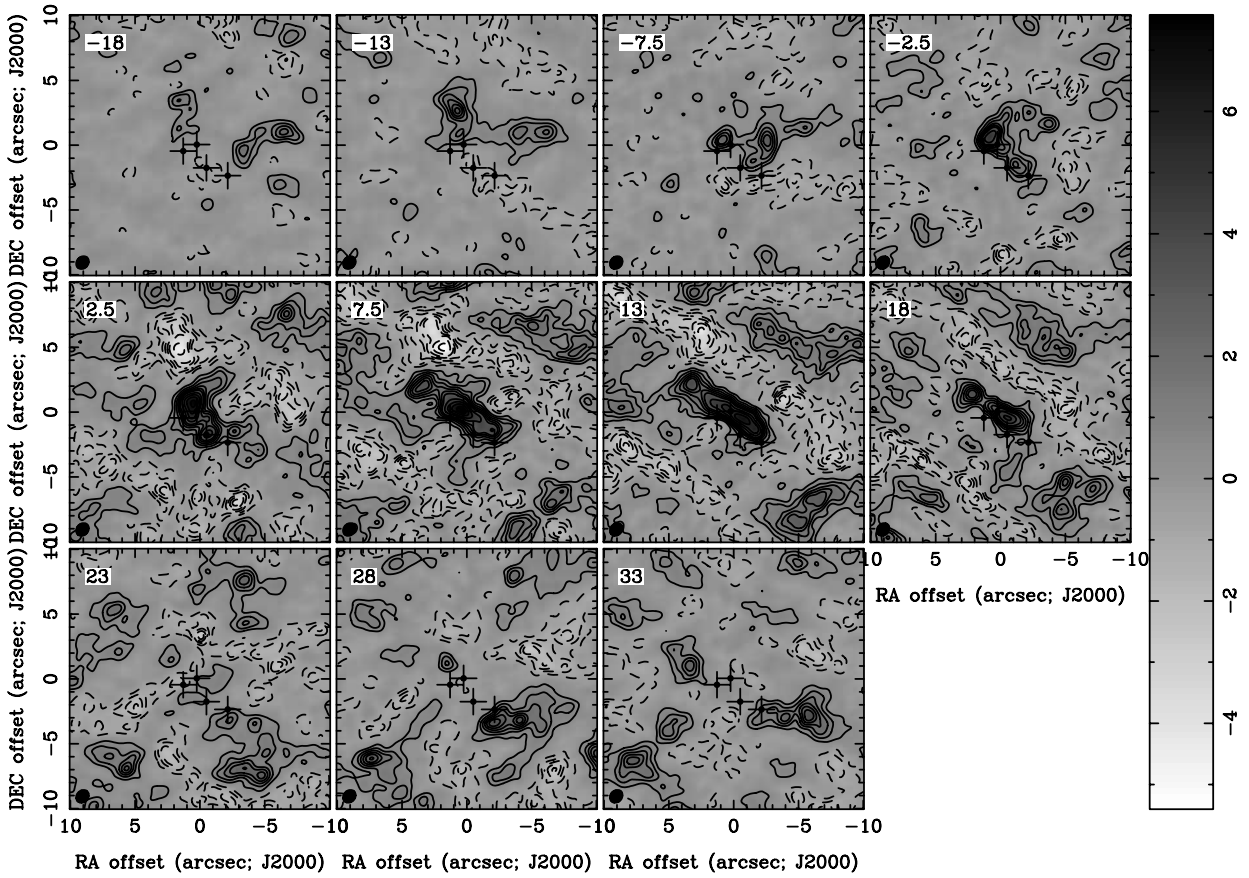

FIG. 8.—^{28}SiO (8–7) channel map in gray scale (the wedge is in units of Jy); positive features are presented in solid lines and negative in dashed lines (contour levels ±0.5, ±1, ±1.5, ±2, ±2.5, ±3, ±4, ±5, 6, and 7 Jy). The channel-center velocities are shown at the top left of each panel; the four dotted crosses mark the positions of source *I*, the hot core, SMA1, and source *n* (see Fig. 1). The synthesized beam is presented at the bottom left of each panel.

close to source *n* does not necessarily imply the opposite. For example, dissociative shocks with velocities >60 km s^{-1} do not produce significant SiO emission (e.g., Flower et al. 1996), and SiO can also be found in distinct bullets further down from the outflow center. However, it remains interesting to note that the SiO emission from sources *I* and *n* is so different. Since source *n* is less deeply embedded than source *I*, either it may have driven an outflow in the past and we might still observe the shocked remnants in H_2O maser emission (Menten & Reid 1995), or the outflow is potentially of a slightly different, perhaps more evolved nature than the ones usually observed in SiO.

Figure 12 shows a comparison of the ^{28}SiO and ^{30}SiO spectrum integrated over the central $4'' \times 4''$ region. Both spectra cover about the same velocity range, and the ^{30}SiO spectrum is only 20% weaker than the main isotopologue ^{28}SiO. This is different from the line ratio observed for these lines with the CSO 10.4 m single-dish telescope. Schilke et al. (1997a) find in their survey a ^{28}SiO/^{30}SiO ratio of about 8, consistent with a ^{28}SiO opacity of 2. It appears that the observed line ratio decreases at higher spatial resolution. However, missing short spacings are a severe problem in comparing fluxes from different species and isotopologues because the spatial filtering affects various species differently. Trying to quantify this effect, we convolved the ^{28}SiO and ^{30}SiO maps to the $20''$ resolution of the CSO observations and compared the resulting peak fluxes. We then performed the same convolution again but this time masking out all negative features. The first approach gives an extreme lower limit to the recovered line intensities because the negative flux caused by the missing large-scale emission is included (Table 4). With these two approaches, we recover between 0.3% and 13% of the ^{28}SiO line flux and between 15% and 49% of the ^{30}SiO line flux. An additional effect caused by the missing short spacings is that the outflow emission is embedded in a larger scale "bowl" of negative emission, which to first order lowers the observed peak fluxes as well. Trying to estimate the distortion of the measured fluxes by this bowl, we find that the main ^{28}SiO line intensity is reduced by approximately 15%, whereas the rarer ^{30}SiO is affected by the bowl to only about 5%. While it is difficult to give exactly how much emission is filtered out in each line, these estimates show that the spatial filtering affects the main isotopologue ^{28}SiO significantly more strongly than its rarer species ^{30}SiO. As outlined in § 2, the missing flux must be distributed over large spatial scales; compared to the approximate missing flux of 3 Jy per synthesized SMA beam for ^{28}SiO (§ 2), this value is considerably lower for ^{30}SiO, between 0.21 and 0.35 Jy per synthesized SMA beam (depending on the SMA ^{30}SiO flux measurement in Table 4). In addition to this, it is likely that the line opacities toward the central $(4'')^2$ are higher than those in the larger region traced by the CSO ($20''$ beam). This would also decrease the observed ^{28}SiO/^{30}SiO ratio. Hence, the observed ^{28}SiO/^{30}SiO ratio of approximately unity is explicable by a combination of spatial filtering and opacity effects.

4.2. CH_3OH *Emission*

The methanol molecule shows by far the most lines within our spectral coverage. We identify 49 transitions from the $v_t = 0$, 1, and 2 states of CH_3OH as well as its isotopologue $^{13}CH_3OH$ (46 and 3, respectively). As shown in Figure 6, the methanol spatial distribution is significantly different from the N-bearing hot core

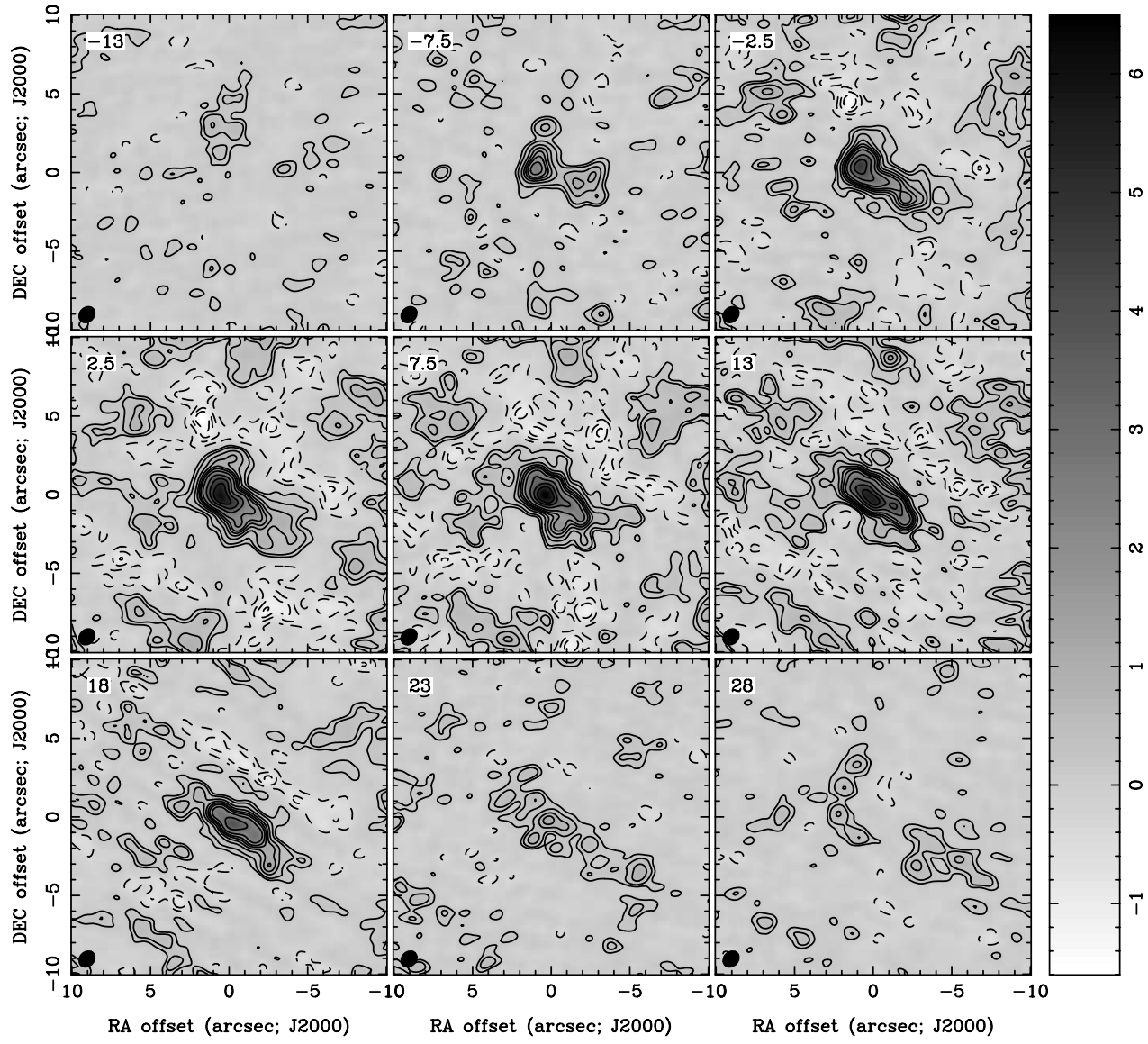

FIG. 9.—^{30}SiO (8–7) channel map in gray scale (the wedge is in units of Jy); positive features are presented in solid lines and negative in dashed lines (contour levels are 0.15, ±0.3, ±0.6, ±0.9, ±1.2, 1.5, 2, 3, 4, and 5 Jy). The channel-center velocities are shown at the top left of each panel; the four dotted crosses mark the positions of source *I*, the hot core, SMA1, and source *n* (see Fig. 1).

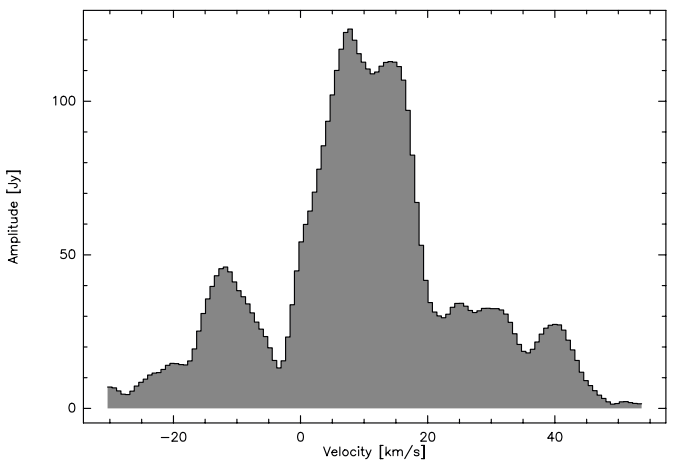

FIG. 10.—Vector-averaged ^{28}SiO (8–7) spectrum observed on a short baseline of ~21 m, with a velocity resolution of 0.7 km s^{-1}.

molecules with a strong additional peak in the southwest toward the compact ridge. We also find that the CH_3OH emission is stronger toward the SMA1 submillimeter continuum peak than toward the strongest submillimeter continuum peak, which usually determines the hot core peak position.

The rich CH_3OH spectra not only provide spatial and kinematic information but also allow possible estimates of the excitation condition of the gas throughout the region. The observed CH_3OH transitions have upper state energy levels spanning from ≈75 to ≈700 K, readily indicating the high-temperature nature of the gas in this region. If we assume that the CH_3OH line emission originates from the same parcels of gas along each line of sight in local thermodynamic equilibrium (LTE; thus having the same size, velocity, and a single temperature), rotational temperatures can be derived by the rotation or population diagram analysis (e.g., Goldsmith & Langer 1999). However, line blending among the CH_3OH transitions as well as with other species complicates the line-intensity estimates and subsequent analysis. To remedy the situation, we estimate the temperature by optimizing

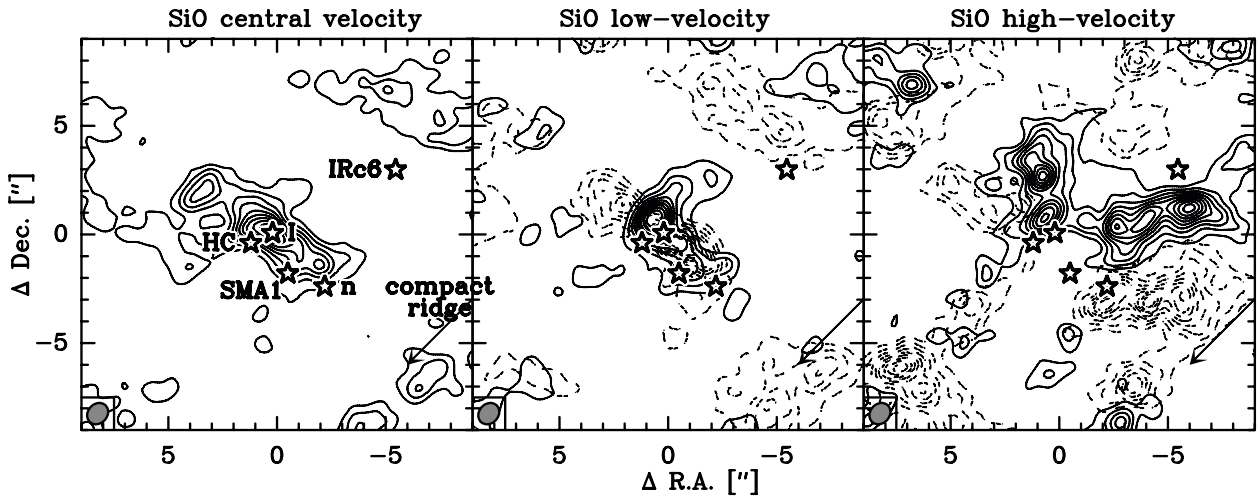

FIG. 11.—^{28}SiO (8–7) images integrated over selected velocity ranges. The left panel presents the ^{28}SiO emission at the central velocities between 5 and 10 km s^{-1}. The middle panel shows the main ^{28}SiO outflow, blue (*solid contours*) [−5, 5] km s^{-1} and red (*dashed contours*) [10, 20] km s^{-1}. The right panel then shows the ^{28}SiO emission integrated over the spectral features at even higher velocities (Fig. 10), blue (*solid contours*) [−18, −5] km s^{-1} and red (*dashed contours*) [23, 35] km s^{-1}. Again, to avoid confusion, negative emission due to missing short spacings is omitted in these plots. Source *I*, the hot core (HC), SMA1, source *n*, IRc6, and the compact ridge are marked in each panel and labeled in the left panel (see Fig. 6). The synthesized beam is presented at the bottom left of each panel.

synthetic spectra to observed spectra, an approach similar to those employed, for example, by Nummelin et al. (1998) and Comito et al. (2005). First, the observed CH_3OH lines toward a particular line of sight are considered to be independent of their intensities, associated only by their relative rest frequency differences. By using the minimum χ^2 algorithm between the synthetic and observed spectra, we fitted all CH_3OH lines simultaneously with Gaussian line profiles to derive common center velocities and linewidths. With the fixed velocities and line widths, the rotational temperatures are then derived via a second χ^2 minimization, matching the synthetic to the observed intensities. In this derivation, the line opacity is assumed to have Gaussian profiles, a beam filling factor is employed, and the background radiation has been ignored.

Figure 13 presents observed and synthetic (fitted) spectra toward the hot core position and a location in the vicinity of the compact ridge but offset from the torsionally excited lines (the position is approximately the center of the HCOOH emission presented in Liu et al. 2002; see also Fig. 14). While the CH_3OH lines from both torsionally ground and excited states are apparent toward the hot core, only transitions from torsionally ground states are noticeable at the latter position. Given that the torsionally excited states require either high densities and temperatures for collisional excitation or strong infrared radiation fields for radiative pumping, the above behavior readily demonstrates variations in excitation conditions at different locations.

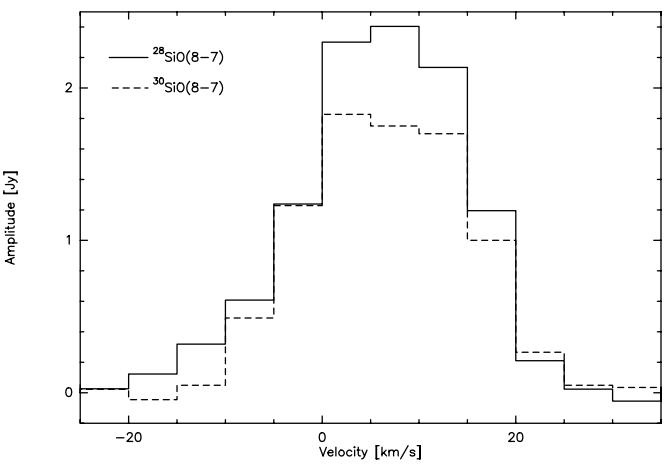

FIG. 12.—^{28}SiO (8–7) (*solid line*) and ^{30}SiO (8–7) (*dashed line*) spectra integrated over the central $4'' \times 4''$ area.

Figure 14 presents the derived rotational temperature structure toward the Orion KL region. To increase the signal-to-noise ratio (S/N), we have smoothed/binned the original 0.″1 pixel images to a larger pixel size of 0.″9, of the order of the beam size. Still, this map gives one of the most detailed spatial pictures of the temperature distribution in this region. The derived rotational temperatures are between 50 and 350 K, with a mean value of ≈150 K over the region. Formal statistical errors from the fitting mostly range between 10 and 50 K. The temperatures we obtained are consistent with previous studies based on (sub)millimeter molecular line emission (e.g., Blake et al. 1987; Wilner et al. 1994; Schilke et al. 1997a; Wilson et al. 2000; Comito et al. 2005) and mid-infrared observations (Gezari et al. 1998). The highest temperature locations are mostly found to be close to the hot core positions such as the main submillimeter continuum peak. In some regions, such as toward the southwest of SMA1 near the compact ridge, lines from the torsionally ground and excited states have similar intensities and thus appear to be optically thick (Fig. 13). In such optically thick cases, the fitting becomes insensitive to the rotational temperature along the particular line of sight. Toward locations where more than half of the CH_3OH lines show fitted opacities >1, we refrained from temperature estimates and blanked the pixels in Figure 14. However, in the optical thick case the apparent intensity (brightness temperature) is directly

TABLE 4
^{28}SiO AND ^{30}SiO LINE INTENSITIES

Line	CSO (20″)[a] (K)	SMA[b] (K)	SMA$_{>0}$[c] (K)	Range (%)
^{28}SiO	34.5	0.1	4.4	0.3–13
^{30}SiO	4.1	0.6	2.0	15–49

[a] From Schilke et al. (1997a).
[b] Convolved to the 20″ CSO beam.
[c] Convolved to the 20″ CSO beam after masking out the negative emission.

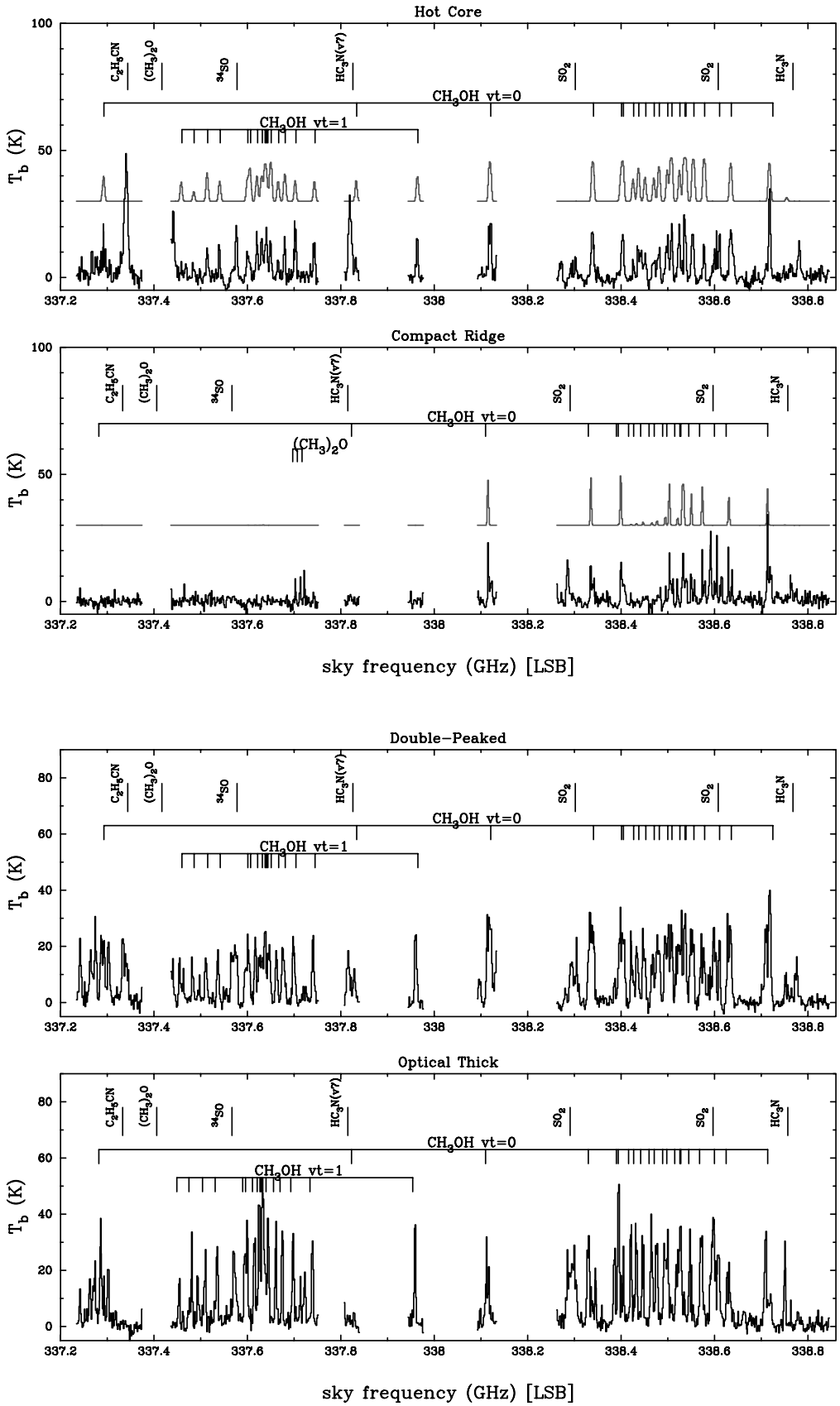

FIG. 13.—CH_3OH spectra toward selected positions in Orion KL. The top two panels show observed spectra in black lines (baselines at intensity 0) and corresponding fits in gray lines (baselines at intensity 2.5) toward the Hot Core and the southern Compact Ridge position marked in Fig. 14. The bottom two panels present spectra that were not possible to fit because they either show double peaks or are optically thick; the positions are also marked in Fig. 14.

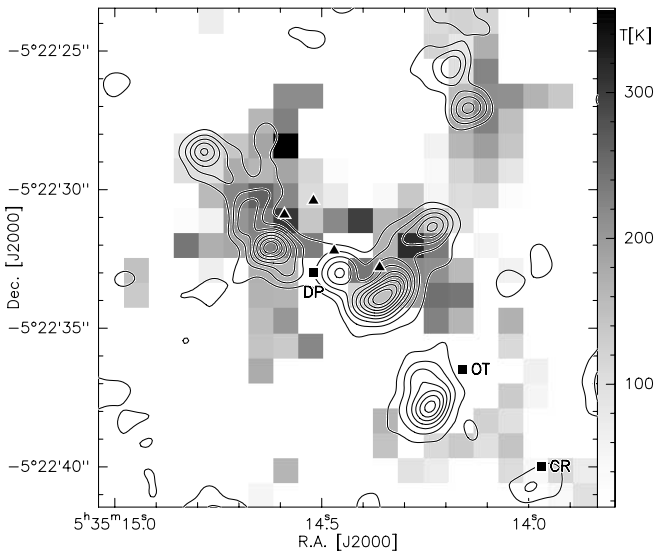

FIG. 14.—Rotational temperatures derived from the whole lower sideband CH_3OH data set are presented in gray scale. The contour overlay shows the same CH_3OH ground state map as shown in Fig. 6. The triangles mark the positions of source *I*, the millimeter continuum peak of the hot core, the continuum peak SMA1, and source *n* (cf. Fig. 1). The squares mark additional positions used to extract the spectra shown in Fig. 13 (CR: [Southern] Compact Ridge [see HCOOH map by Liu et al. 2002], OT: optical thick, DP: double-peaked). To calculate the rotational temperature map, we binned the original 0.″1 pixel line maps to a larger pixel size of 0.″9 (to increase the S/N). Therefore, the temperature map gives values over a bit larger spatial area than the unbinned, higher spatial-resolution CH_3OH line map.

related to the true brightness temperature, differing only by the filling factor. For example, using the averaged temperature of 150 K and typical observed peak intensity of 4 Jy beam^{-1} toward such optically thick directions, we find filling factors of 0.3 or less in the smoothed data cube. For positions where the spectral fitting is successful, the filling factors are even smaller, 0.14 on average. Such small filling factors may appear somewhat surprising, given past studies. Comito et al. (2005), for example, adopted a source size of 10″ for CH_3OH emission but also obtained a similar rotational temperature. One expects that, when imaged at a higher angular resolution, the CH_3OH emission would be resolved and thus fill the smaller beam. The fact that we find rotational temperatures comparable to past studies but with filling factor less than unity even for the optically thick lines suggests that a significant amount of CH_3OH emission is missing and the observed hot CH_3OH gas is actually clumpy. Indeed, smoothing the data to the 20″ CSO beam and comparing these spectra with the single-dish observations by Schilke et al. (1997a), as much as 90% of the integrated CH_3OH flux is resolved out by the interferometer. Since the spatial filtering affects various CH_3OH lines differently, this has to be taken into account as well. As discussed in §§ 2 and 4.1, the missing flux has to be distributed over large spatial scales, and the more interesting parameter is the missing flux per synthesized beam. Estimating the latter values, we find that the CH_3OH missing flux per synthesized SMA beam is in the worst case at a 10%–20% level, within the calibration uncertainty. Therefore, it should not affect the temperature determination significantly.

We note that there are a few caveats in our synthetic spectral fitting process that do not always result in satisfactory fitted spectra. As mentioned above, the fitting process fails toward optically thick regions. Moreover, at some positions, the CH_3OH lines appear to be double-peaked, or a velocity offset between the torsionally ground state and excited transitions is noticeable (Fig. 13). If various kinematic components are present, our fitting process often fails to converge. In addition, (minor) disagreement between the observed and fitted spectra is not limited to the above cases but also present in the two top spectra of Figure 13. Since all transitions were observed simultaneously, calibration errors due to poor pointing or amplitude scaling are likely to be canceled out. Such deviations therefore suggest that additional non-LTE effects are at work. Furthermore, radiative pumping of the torsionally excited as well as the ground state transitions also needs to be considered, although collisional excitation is likely to dominate in high-density regions like the Orion KL (Menten et al. 1986). A full statistical equilibrium analysis such as that suggested by Leurini et al. (2004), which is outside the scope of this paper, and the inclusion of torsionally excited states would be an interesting next step to investigate these effects.

4.3. *Vibrational Excited Emission*

SMA1.—The three vibrationally/torsionally excited lines in the survey (CH_3OH, SO_2, HC_3CN) all show strong emission toward the submillimeter continuum source SMA1 (Fig. 6). Since these lines are usually excited by infrared radiation, this emission indicates a deeply embedded infrared source at the position of SMA1. Similar conclusions were drawn by de Vicente et al. (2002) from lower spatial resolution Plateau de Bure observations of vibrational excited HC_3N (10–9). Solely on the basis of the submillimeter continuum study, we could not judge well whether SMA1 is an independent protostellar source or whether it is an extension of the hot core (Beuther et al. 2004). These vibrationally excited line studies support the independent protostellar object interpretation for SMA1. Because SMA1 is detected neither at infrared nor at centimeter wavelength, it is likely one of the youngest sources of the evolving cluster.

The Compact Ridge.—The torsionally excited CH_3OH is also observed toward the compact ridge. We find only weak, vibrationally excited SO_2 and no HC_3N emission in this region. It is possible that an additional embedded infrared source exists in the region of the compact ridge, but we do not detect any emission above the noise in the 865 μm continuum there (Beuther et al. 2004). In contrast to this, Blake et al. (1996) detected weak millimeter continuum emission in that region. However, their millimeter continuum map does not show a strong peak but is more broadly distributed. The compact ridge is believed to be the interface region between one (or more?) of the molecular outflows with the dense ambient gas (e.g., Blake et al. 1987; Liu et al. 2002). Since torsionally excited CH_3OH can also be produced in regions of extremely high densities (critical densities of the order of 10^{10} cm^{-3}), it might also be possible that the CH_3OH $v_t = 1$, 2 lines are excited in this interface region without an embedded infrared source.

5. CONCLUSION

The presented observations comprise a large set of molecular line data (∼145 lines from ∼24 species, isotopologues, and vibrational excited states) taken simultaneously during only two observing nights. The large number of observed CH_3OH lines (46) with $v_t = 0$, 1, and 2 are a powerful tool to derive physical parameters (e.g., temperatures) of the molecular gas, and we find temperatures between 50 and 350 K throughout the region.

The SiO lines trace the collimated low-velocity molecular jet emanating from source *I*, as well as larger scale emission likely associated with a different outflow. In contrast to previously reported ground state ^{28}SiO (1–0) and (2–1) maser emission close to source *I*, we do not find detectable ^{28}SiO (8–7) maser emission there. Since source *n* is weak in the outflow-tracing

SiO emission, this could indicate that it may currently drive no molecular outflow anymore.

Comparing different molecular species, for example, nitrogen-, oxygen-, and sulphur-bearing molecules, we find strong chemical gradients over the observed region. For example, source *I* exhibits mainly SiO emission, whereas the hot core is especially strong in nitrogen-bearing molecules like CH_3CN. The strongest emission features of most oxygen-bearing molecules are south of the hot core toward the so-called compact ridge. These differences have important implications for studies of lower spatial-resolution and/or of sources at larger distances. For example, analyzing the data of a typical massive star-forming region at approximately 4 kpc distance and deriving spatially averaged temperatures from the CH_3OH data does not necessarily imply that the same temperatures can be attributed to the (sub)millimeter dust continuum cores. Furthermore, the imaging of spectral lines can be used as an additional tool for line identifications. Since new interstellar molecular line identifications get more complicated for large and complex molecules (see, e.g., the controversy about glycine; Kuan et al. 2003; Snyder et al. 2005), imaging each molecular line and comparing their spatial distributions is an important consistency check for rigorous line identifications.

All vibrationally/torsionally excited lines show strong emission toward the submillimeter continuum peak SMA1. Because this emission is usually excited by infrared emission, it supports the notion that the recently identified source SMA1 is likely of protostellar nature.

This data set is particularly rich and has potential for follow-up investigations. To mention just a couple: imaging and potentially identifying the low-level emission peaks, or better constraining the underlying physical processes, which are responsible for the observed chemical gradients, is of great interest.

We would like to thank everyone at the SMA for their great efforts over many years to get the instrument going! An additional thank you goes to the referee, Peter Schilke, for detailed comments that improved the paper. H. B. acknowledges financial support by the Emmy-Noether-Program of the Deutsche Forschungsgemeinschaft (DFG grant BE2578/1).

REFERENCES

Allen, D. A., & Burton, M. G. 1993, Nature, 363, 54
Beuther, H., et al. 2004, ApJ, 616, L31
Blake, G. A., Sutton, E. C., Masson, C. R., & Phillips, T. G. 1987, ApJ, 315, 621
Blake, G. A., et al. 1996, ApJ, 472, L49
Cesaroni, R., et al. 1999, A&A, 345, 949
Chandler, C. J., & de Pree, C. G. 1995, ApJ, 455, L67
Chernin, L. M., & Wright, M. C. H. 1996, ApJ, 467, 676
Chrysostomou, A., et al. 1997, MNRAS, 289, 605
Comito, C., Schilke, P., Phillips, T. G., Lis, D. C., Motte, F., & Mehringer, D. 2005, ApJS, 156, 127
de Vicente, P., Martín-Pintado, J., Neri, R., & Rodríguez-Franco, A. 2002, ApJ, 574, L163
Dougados, C., Lena, P., Ridgway, S. T., Christou, J. C., & Probst, R. G. 1993, ApJ, 406, 112
Flower, D. R., Pineau des Forets, G., Field, D., & May, P. W. 1996, MNRAS, 280, 447
Genzel, R., & Stutzki, J. 1989, ARA&A, 27, 41
Gezari, D. Y. 1992, ApJ, 396, L43
Gezari, D. Y., Backman, D. E., & Werner, M. W. 1998, ApJ, 509, 283
Goldsmith, P. F., & Langer, W. D. 1999, ApJ, 517, 209
Greenhill, L. J., Gezari, D. Y., Danchi, W. C., Najita, J., Monnier, J. D., & Tuthill, P. G. 2004a, ApJ, 605, L57
Greenhill, L. J., Reid, M. J., Chandler, C. J., Diamond, P. J., & Elitzur, M. 2004b, in IAU Symp. 221, Star Formation at High Angular Resolution, ed. M. Burton, R. Jayawardhana, & T. Bourke (San Francisco: ASP), 155
Gueth, F., & Guilloteau, S. 1999, A&A, 343, 571
Ho, P. T. P., Moran, J. M., & Lo, K. Y. 2004, ApJ, 616, L1
Kreysa, E., et al. 1998, Proc. SPIE, 3357, 319
Kuan, Y., Charnley, S. B., Huang, H., Tseng, W., & Kisiel, Z. 2003, ApJ, 593, 848
Leurini, S., Schilke, P., Menten, K. M., Flower, D. R., Pottage, J. T., & Xu, L.-H. 2004, A&A, 422, 573
Liu, S., Girart, J. M., Remijan, A., & Snyder, L. E. 2002, ApJ, 576, 255
Lovas, F. 2004, J. Phys. Ref. Data, 33, 177
Menten, K. M., & Reid, M. J. 1995, ApJ, 445, L157
Menten, K. M., Walmsley, C. M., Henkel, C., Wilson, T. L., Snyder, L. E., Hollis, J. M., Lovas, F. J. 1986, A&A, 169, 271
Müller, H. S. P., Thorwirth, S., Roth, D. A., & Winnewisser, G. 2001, A&A, 370, L49
Nummelin, A., Dickens, J. E., Bergman, P., Hjalmarson, Aa., Irvine, W. M., Ikeda, M., & Ohishi, M. 1998, A&A, 337, 275
Plambeck, R. L., Wright, M. C. H., Mundy, L. G., & Looney, L. W. 1995, ApJ, 455, L189
Poynter, R. L., & Pickett, H. M. 1985, Appl. Opt., 24, 2235
Schilke, P., Benford, D. J., Hunter, T. R., Lis, D. C., & Phillips, T. G. 2001, ApJS, 132, 281
Schilke, P., Groesbeck, T. D., Blake, G. A., & Phillips, T. G. 1997a, ApJS, 108, 301
Schilke, P., Walmsley, C. M., Pineau des Forets, G., & Flower, D. R. 1997b, A&A, 321, 293
Schultz, A. S. B., et al. 1999, ApJ, 511, 282
Shuping, R. Y., Morris, M., & Bally, J. 2004, AJ, 128, 363
Snyder, L. E., et al. 2005, ApJ, 619, 914
Stolovy, S. R., et al. 1998, ApJ, 492, L151
Sutton, E. C., Blake, G. A., Masson, C. R., & Phillips, T. G. 1985, ApJS, 58, 341
Wilner, D. J., Wright, M. C. H., & Plambeck, R. L. 1994, ApJ, 422, 642
Wilson, T. L., Gaume, R. A., Gensheimer, P., & Johnston, K. J. 2000, ApJ, 538, 665
Wright, M. C. H., Plambeck, R. L., Mundy, L. G., & Looney, L. W. 1995, ApJ, 455, L185
Wright, M. C. H., Plambeck, R. L., & Wilner, D. J. 1996, ApJ, 469, 216